

On the Spatial Segregation of Helicity by Inertial Waves in Dynamo Simulations and Planetary Cores

P. A. Davidson and A. Ranjan

Dept. Engineering, University of Cambridge, Trumpington Street, Cambridge, UK.

Revised, March, 2018.

Summary

The distribution of kinetic helicity in a dipolar planetary dynamo is central to the success of that dynamo. Motivated by the helicity distributions observed in numerical simulations of the earth's dynamo, we consider the relationship between the kinetic helicity, $h = \mathbf{u} \cdot \nabla \times \mathbf{u}$, and the buoyancy field that acts as a source of helicity. We show that, in the absence of a magnetic field, helicity evolves in accordance with the equation $\partial h / \partial t = -\nabla \cdot \mathbf{F} + S_h$, where the flux, \mathbf{F} , represents the transport of helicity by inertial waves, and the helicity source, S_h , involves the product of the buoyancy and the velocity fields. In the numerical simulations it is observed that the helicity outside the tangent cylinder is predominantly negative in the north and positive in the south, a feature which the authors had previously attributed to the transport of helicity by waves (Davidson & Ranjan, 2015). It is also observed that there is a strong spatial correlation between the distribution of h and of S_h , with S_h also predominantly negative in the north and positive in the south. This correlation tentatively suggests that it is the *in situ* generation of helicity by buoyancy that establishes the distribution of h outside the tangent cylinder, rather than the dispersal of helicity by waves, as had been previously argued by the authors. However, although h and S_h are strongly correlated, there is no such correlation between $\partial h / \partial t$ and S_h , as might be expected if the distribution of h were established by an *in situ* generation mechanism. We explain these various observations by showing that inertial waves interact with the buoyancy field in such a way as to induce a source S_h which has the same sign as the helicity in the local wave flux, and that the sign of h is simply determined by the direction of that flux. We conclude that the observed distributions of h and S_h outside the tangent cylinder are consistent with the transport of helicity by waves.

1. Introduction

One of the major advances in convection-driven dynamos over the last decade has been the ability of the numerical simulations to reproduce some of the observed features of the earth's magnetic field, such as a strongly dipolar magnetic field aligned with the rotation axis, occasional reversals in polarity, and a slow westward drift of the surface magnetic field (Christensen, 2010). This is all the more astonishing as the parameter regime in the numerical experiments is very far from that in the core of the earth. For example, the simulations are much too viscous, typically by a factor of 10^9 as measured by the Ekman number, and substantially underpowered, as measured by the ratio of the Rayleigh number to the critical Rayleigh number at which convection first sets in (Christensen & Wicht, 2007, Christensen, 2011). There is, therefore, a growing need to understand exactly what dynamical mechanisms these numerical experiments embrace which allows them to capture planet-like behaviour, despite the fact that many aspects of the simulations are distinctly not planet like.

It was recognised early in dynamo theory that an important ingredient of a dipolar planetary dynamo is the breaking of reflectional symmetry (Moffatt, 1978), and in the numerical simulations of such dynamos this usually takes the form of an abundance of kinetic helicity, $h = \mathbf{u} \cdot \nabla \times \mathbf{u} = \mathbf{u} \cdot \boldsymbol{\omega}$, in the convective flow (Roberts & King, 2013). Moreover, an efficient dynamo requires that the mean helicity is spatially segregated, being of one sign in the northern hemisphere and another sign in the south. Precisely such an asymmetric distribution in the azimuthally-averaged helicity was observed quite early in the numerical simulations (Olson, Christensen, & Glatzmaier, 1999), and indeed it occurs even in the absence of a magnetic field (Glatzmaier & Olson, 1993, Kitauchi, Araki & Kida, 1997). In particular, outside the tangent cylinder (an imaginary cylinder that circumscribes the solid inner core and is parallel with the rotation vector, $\boldsymbol{\Omega}$), the helicity is observed to be negative in the north and positive in the south. This is important because nearly all of the current numerical dynamos operate outside the tangent cylinder (Christensen, 2011). So, two important questions are: what basic mechanism is responsible for the generation and subsequent spatial segregation of helicity in the numerical simulations, and why is it predominantly negative in the north and positive in the south (outside the tangent cylinder)? To date, these questions remain unanswered.

The production and segregation of helicity was attributed to Ekman pumping in some of the early simulations (Roberts & King, 2013, Kono, Sakuraba & Ishida,

2000), but these simulations were particularly viscous and weakly forced, and this has now been largely abandoned as a realistic mechanism. For example, it is not the primary source of helicity in slightly less viscous simulations (Olson, Christensen, & Glatzmaier, 1999), it plays almost no role whatsoever in the most recent low-Ekman number numerical simulations (Schaeffer *et al*, 2017), and numerical simulations involving slip boundary conditions, in which there can be no Ekman pumping, also produce dipolar dynamos (Kageyama, Watanabe & Sato, 1993, Yadav, Gastine & Christensen, 2013). Moreover, Ekman pumping is unlikely to play any role at all in planetary cores, where the Ekman number is tiny, $\sim 10^{-15}$ in the case of the earth.

Given that the earth rotates rapidly with a low convective Rossby number, $Ro = u/\Omega l \ll 1$, it has long been recognised that an alternative source of helicity may be the propagation of helical waves supported by the Coriolis force, (Moffatt, 1970, Olson, 1981). The point is that, while a low value of Ro demands that $\mathbf{u} \cdot \nabla \mathbf{u}$ is much weaker than the Coriolis force, we have no right to similarly neglect $\partial \mathbf{u} / \partial t$, as there is no *a priori* reason why the time derivative should scale on the convective time, and as soon as we allow for a non-negligible $\partial \mathbf{u} / \partial t$, waves are inevitable. This idea was taken up again in Davidson (2014) and Davidson & Ranjan (2015), who focussed particularly on the simplest type of helical wave – inertial waves. The hypothesis put forward in Davidson (2014) and Davidson & Ranjan (2015) is that most planets are rapid rotators and so are natural wave-bearing systems which are almost certainly awash with helical waves, such as inertial waves and magnetostrophic waves. In particular, it is argued that fast inertial waves are required to maintain the approximate geostrophy observed in the simulations, a quasi-geostrophy that is maintained despite the chaotic evolution of the thermal forcing and the turbulent nature of the resulting velocity field. Moreover, outside the tangent cylinder the temperature perturbations and buoyancy flux, which act as triggers for helical waves, are observed to be concentrated in and around the equatorial plane. This was noticed as early as Gilman (1977) and then later by Glatzmaier & Olson (1993). This is illustrated in Figure 1(a), which is taken from Sakuraba & Roberts (2009) and shows the computed radial velocity in one of their simulations. It is also evident in Figure 1(b), which is from Ranjan *et al* (2018) and shows the computed r.m.s. azimuthal temperature gradient, averaged in the azimuth. In both of these cases the primary source of excitation for waves lies in the equatorial regions. This is significant because upward propagating

helical waves, either inertial or magnetostrophic waves, are known to carry negative helicity, while downward propagating helical waves carry positive helicity (Moffatt, 1978). So waves triggered in and around the equatorial plane will tend to support negative helicity in the north and positive helicity in the south, exactly as seen in the numerical simulations (Figure 1(c)), and exactly as required for dynamo action.

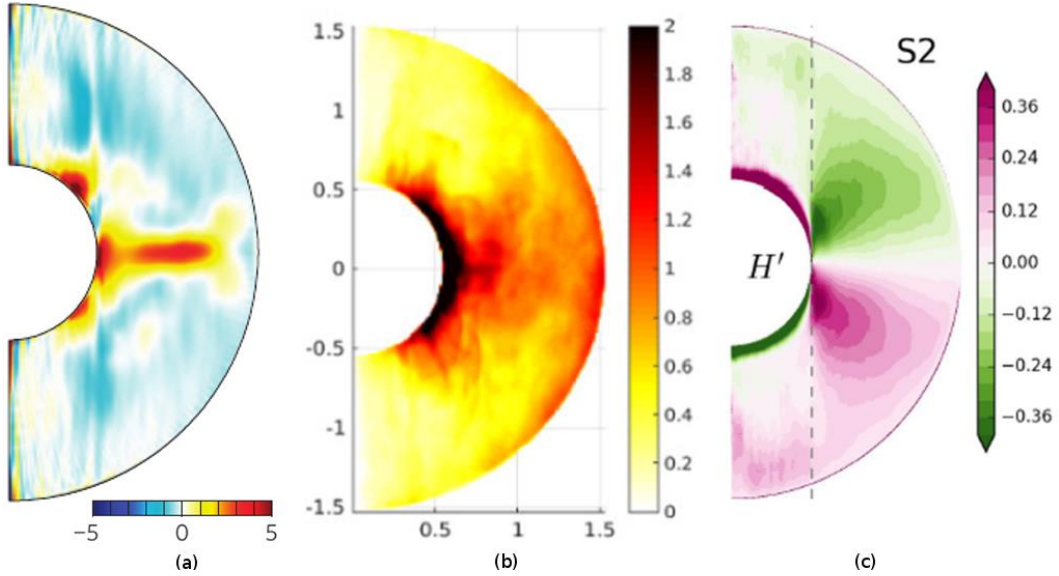


Figure 1. (a) The computed radial velocity in one of the simulations of Sakuraba & Roberts (2009). (b) The r.m.s. azimuthal temperature gradient, averaged in the azimuth, in the simulation of Ranjan *et al* (2018). (c) The helicity distribution in a simulation by Schaeffer *et al* (2017).

There is a second, intriguing feature of the numerical simulations that requires some explanation. As noted in Davidson & Ranjan (2015), it is possible to write a low- Ro evolution equation for the helicity of the form

$$\frac{\partial}{\partial t}(\mathbf{u} \cdot \boldsymbol{\omega}) = -\nabla \cdot \mathbf{F} + S_h. \quad (1.1)$$

The origins and interpretation of this equation are spelt out in §2, where it is shown that \mathbf{F} is a wave flux involving the Coriolis force, and hence $\boldsymbol{\Omega}$, while the source term, S_h , is a function of $\mathbf{u}(\mathbf{x}, t)$ and of those buoyancy fluctuations which act as triggers for helical waves. A comparison of the azimuthally averaged distributions of h and S_h in a numerical dynamo is shown in Figure 2 (a, b), where panel (a) is taken from Ranjan

et al (2018) and panel (b) has been calculated from the same data set. It is extraordinary how close the azimuthally averaged spatial distributions of h and S_h are. At first sight this argues for an *in situ* generation of helicity, such as the quasi-static mechanism suggested by Hide (1976), rather than the dispersal of helicity by waves. Curiously, though, no such correlation is observed between $\partial h/\partial t$ and S_h in the same numerical simulation (Figure 2 c). This suggests that there may be an alternative explanation for the observed correlation between h and S_h , and we shall argue here that this is indeed the case. Specifically, we shall show the source term in (1.1) automatically adjusts to take the same sign as the prevailing helical wave flux. That is to say, S_h is not independently prescribed, but is itself shaped by the wave dynamics.

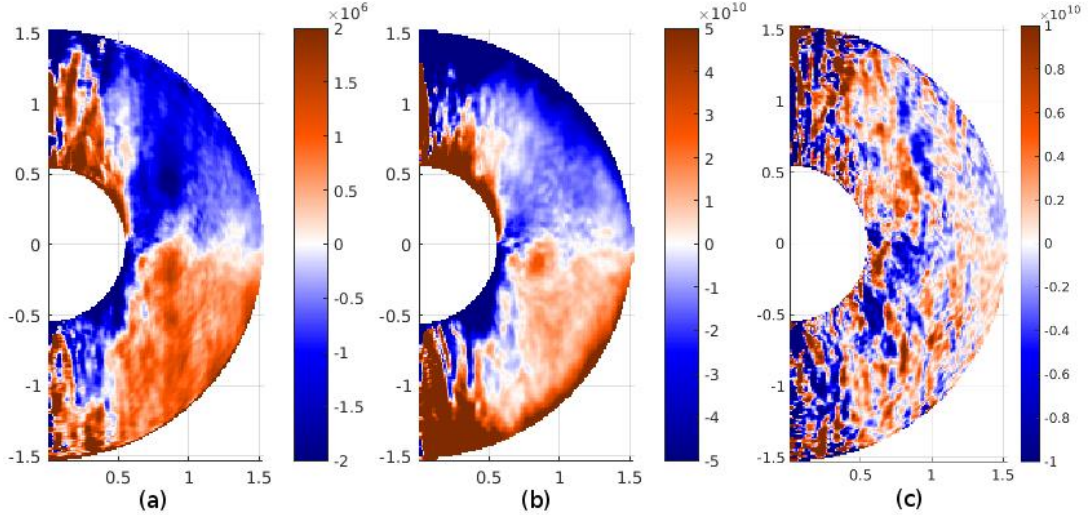


Figure 2. A comparison of the azimuthally averaged values of h , S_h and $\partial h/\partial t$ in equation (1.1). Panel (a) is taken from Ranjan *et al* (2018) and (b, c) have been calculated from the same dataset.

Because of the presence of both an ambient magnetic field and a background rotation, there are several classes of helical waves which might exist in the core of a planet. However, these share many common features and differ mostly in their time scales (Moffatt, 1978). Consequently, we shall follow Davidson & Ranjan (2015) and focus on the simplest case – that of inertial waves. In the parlance of dynamo theory, we consider the weak-field regime. Our primary task is to test the hypothesis that the antisymmetric distribution in h observed in the numerical simulations, as well as the

spatial correlation between h and S_h in (1.1), could arise from the spontaneous emission of inertial waves from buoyant anomalies. Because the numerical simulations exhibit highly complex dynamics, with many distinct physical processes occurring simultaneously on multiple time scales, we restrict ourselves to a sequence of idealised model problems, designed to expose the underlying dynamics.

2. The Equations Governing the Dispersal of Helicity from a Localised Source of Buoyancy

2.1 Inertial Waves at Low Rossby Number

We consider a rapidly-rotating, Boussinesq fluid at low Rossby number, $\text{Ro} = u/2\Omega\ell \ll 1$, in which motion is driven by density anomalies. The governing equations of motion in the rotating frame of reference are

$$\frac{\partial \mathbf{u}}{\partial t} = 2\mathbf{u} \times \boldsymbol{\Omega} - \nabla(p/\rho) + \mathcal{G}\mathbf{g} + \nu \nabla^2 \mathbf{u}, \quad (2.1)$$

$$\nabla \cdot \mathbf{u} = 0, \quad (2.2)$$

where $\boldsymbol{\Omega} = \Omega \hat{\mathbf{e}}_z$ is the background rotation, p is pressure, ν the viscosity, ρ the background density, \mathbf{g} is gravity, $\mathcal{G} = \rho'/\rho$, and ρ' is the perturbation in density. We have in mind cases where \mathbf{g} is perpendicular to $\boldsymbol{\Omega}$, reminiscent of a buoyant anomaly sitting near the equatorial plane of the earth's core, and we take ρ' to be negative, in line with the notion of buoyant anomalies floating out towards the mantle in the core.

If we introduce a solenoidal vector potential, \mathbf{a} , for the velocity, $\mathbf{u} = \nabla \times \mathbf{a}$, then we may rewrite (2.1), and its curl, in the alternative form,

$$\frac{\partial \mathbf{u}}{\partial t} = 2\boldsymbol{\Omega} \cdot \nabla \mathbf{a} - \nabla(p^*/\rho) + \mathcal{G}\mathbf{g} + \nu \nabla^2 \mathbf{u}, \quad (2.3)$$

$$\frac{\partial \boldsymbol{\omega}}{\partial t} = 2\boldsymbol{\Omega} \cdot \nabla \mathbf{u} + \nabla \mathcal{G} \times \mathbf{g} + \nu \nabla^2 \boldsymbol{\omega}, \quad (2.4)$$

where

$$\nabla^2(p^*/\rho) = \nabla \cdot (\mathcal{G}\mathbf{g}). \quad (2.5)$$

The buoyancy field, \mathcal{G} , is assumed to be advected by a simple advection diffusion equation, with a diffusivity κ equal to that of the kinematic viscosity. From (2.1) we see that $u \sim \mathcal{G}g/\Omega$, and so a characteristic Rossby number is $\text{Ro} = \mathcal{G}_0 g / 2\Omega^2 \delta$,

where ϑ_0 is a characteristic density fluctuation and δ is a typical length-scale for the buoyancy field.

We are interested in how energy and helicity disperse from localised buoyancy sources at low Ekman numbers. In the absence of viscosity, and away from buoyancy sources, (2.3) supports inertial waves governed by the wave-like equation

$$\frac{\partial^2}{\partial t^2} (\nabla^2 \mathbf{u}) + 4(\boldsymbol{\Omega} \cdot \nabla)^2 \mathbf{u} = \mathbf{0}, \quad (2.6)$$

which allows for plane waves of the form $\mathbf{u} = \hat{\mathbf{u}} \exp[j(\mathbf{k} \cdot \mathbf{x} - \varpi t)]$. These have the dispersion relationship

$$\varpi = \pm 2(\mathbf{k} \cdot \boldsymbol{\Omega})/k, \quad k = |\mathbf{k}|, \quad (2.7)$$

with $0 \leq \varpi \leq 2\Omega$ and the lowest frequency corresponding to horizontal wave-vectors, $\mathbf{k} \cdot \boldsymbol{\Omega} = 0$. The group velocity of inertial waves is then

$$\mathbf{c}_g = \frac{\partial \varpi}{\partial k_i} = \pm 2 \frac{\mathbf{k} \times (\boldsymbol{\Omega} \times \mathbf{k})}{|\mathbf{k}|^3} = \pm 2 \frac{k^2 \boldsymbol{\Omega} - (\mathbf{k} \cdot \boldsymbol{\Omega}) \mathbf{k}}{|\mathbf{k}|^3}. \quad (2.8)$$

Note, in particular, that

$$\mathbf{c}_g \cdot \boldsymbol{\Omega} = \pm 2k^{-3} [k^2 \Omega^2 - (\mathbf{k} \cdot \boldsymbol{\Omega})^2], \quad (2.9)$$

which tells us that the positive sign in (2.7) corresponds to wave energy travelling upward, while the negative sign corresponds to energy propagating downward.

Note also that low-frequency waves have a group velocity of $\mathbf{c}_g = \pm 2\boldsymbol{\Omega}/k$, and so $u/c_g \sim \text{Ro}$. It follows that, at low Ro, the buoyancy field, and hence p^* , may be regarded as quasi-static on the timescale of the wave dispersion. Inverting (2.5) tells us that this quasi-static pressure field falls off with distance as $\nabla p^* \sim |\mathbf{x}|^{-3}$ from a localised source of buoyancy. This is faster than the radiation field, which falls as $|\mathbf{u}| \sim |\mathbf{x}|^{-1}$ for on-axis radiation (radiation parallel to $\pm \boldsymbol{\Omega}$) and $|\mathbf{u}| \sim |\mathbf{x}|^{-3/2}$ for off-axis radiation (see Davidson *et al*, 2006, and Davidson, 2013).

Inertial waves have a non-zero helicity, $h = \mathbf{u} \cdot \boldsymbol{\omega}$. This follows from (2.4) combined with the dispersion relationship (2.7), which yields $\hat{\boldsymbol{\omega}} = \mp |\mathbf{k}| \hat{\mathbf{u}}$, where $\hat{\boldsymbol{\omega}}$ is the amplitude of the vorticity in the wave. Evidently the vorticity and velocity fields are parallel and in phase, and so monochromatic inertial waves have maximum possible helicity, with the positive sign in (2.9) corresponding to negative helicity,

and the negative sign to positive helicity (Moffatt, 1978). Although this argument applies only to a single Fourier mode, wave packets containing a range of wavenumbers also have a high relative helicity, and of the sign expected for a monochromatic wave (Davidson & Ranjan, 2015, Ranjan, 2017). Thus, when wave packets disperse from a localised disturbance, waves with negative helicity propagate upward, $\mathbf{c}_g \cdot \boldsymbol{\Omega} > 0$, while those with positive helicity travel downward, $\mathbf{c}_g \cdot \boldsymbol{\Omega} < 0$.

2.2 An Inviscid Evolution Equation for Helicity.

We are interested in how helicity disperses from localised sources of buoyancy. As noted in Davidson & Ranjan (2015), we can obtain an evolution equation for h by taking the dot product of $\boldsymbol{\omega}$ with (2.3), the product of \mathbf{u} with (2.4), and then adding the two equations. Ignoring viscosity, this yields

$$\frac{\partial}{\partial t}(\mathbf{u} \cdot \boldsymbol{\omega}) = \left\{ \boldsymbol{\Omega} \cdot \nabla(\mathbf{u}^2) + (2\boldsymbol{\Omega} \cdot \nabla \mathbf{a}) \cdot \boldsymbol{\omega} \right\} - \nabla \cdot (p^* \boldsymbol{\omega} / \rho) + \mathbf{u} \cdot (\nabla \mathcal{G} \times \mathbf{g}) + \boldsymbol{\omega} \cdot (\mathcal{G} \mathbf{g}). \quad (2.10)$$

The two terms arising from the Coriolis force may be rewritten as a divergence,

$$\boldsymbol{\Omega} \cdot \nabla(\mathbf{u}^2) + (2\boldsymbol{\Omega} \cdot \nabla \mathbf{a}) \cdot \boldsymbol{\omega} = \nabla \cdot \left((2\mathbf{u}^2) \boldsymbol{\Omega} + \mathbf{u} \times (2\boldsymbol{\Omega} \cdot \nabla \mathbf{a}) \right), \quad (2.11)$$

while it will be convenient to rewrite the source terms involving buoyancy as

$$\mathbf{u} \cdot (\nabla \mathcal{G} \times \mathbf{g}) + \boldsymbol{\omega} \cdot (\mathcal{G} \mathbf{g}) = \nabla \cdot (\mathbf{u} \times (\mathcal{G} \mathbf{g})) + 2\mathbf{g} \cdot (\mathbf{u} \times \nabla \mathcal{G}). \quad (2.12)$$

Our evolution equation for helicity can therefore be written symbolically as

$$\frac{\partial}{\partial t}(\mathbf{u} \cdot \boldsymbol{\omega}) = -\nabla \cdot \mathbf{F} + S_h, \quad (2.13)$$

where the flux, \mathbf{F} , and helicity source, S_h , are

$$\mathbf{F} = -(2\mathbf{u}^2) \boldsymbol{\Omega} - 2\mathbf{u} \times (\boldsymbol{\Omega} \cdot \nabla \mathbf{a}) + p^* \boldsymbol{\omega} / \rho, \quad (2.14)$$

and

$$S_h = S_1 + S_2 = \nabla \cdot (\mathbf{u} \times (\mathcal{G} \mathbf{g})) + 2\mathbf{g} \cdot (\mathbf{u} \times \nabla \mathcal{G}). \quad (2.15)$$

Note that S_1 integrates to zero over a spherical domain, though S_2 need not. We shall now examine the flux, \mathbf{F} , and source, S_h , individually.

2.3 The Flux Term in the Helicity Equation.

Well removed from a localised source of buoyancy the quasi-static modified pressure is weak, $p^* \sim |\mathbf{x}|^{-2}$, and so, to leading order in $|\mathbf{x}|^{-1}$, equations (2.13) and (2.14) can be approximated by

$$\frac{\partial}{\partial t}(\mathbf{u} \cdot \boldsymbol{\omega}) = -\nabla \cdot \mathbf{F}, \quad \mathbf{F} \approx -(2\mathbf{u}^2)\boldsymbol{\Omega} - \mathbf{u} \times \frac{\partial \mathbf{u}}{\partial t}. \quad (2.16)$$

Moreover, we shall see in §3 that dispersion from a localised buoyancy source is usually dominated by low-frequency wave packets, $\mathbf{k} \cdot \boldsymbol{\Omega} \approx 0$, and in such cases $\omega \ll \Omega$, so that the helicity flux is simply $\mathbf{F} \approx -(2\mathbf{u}^2)\boldsymbol{\Omega}$. This is consistent with upward propagating wave packets carrying with them negative helicity and downward propagating wave packets transporting positive helicity. To see why this is so, suppose the buoyancy source is localised near the plane $z = 0$, say confined to the region $-\delta < z < \delta$. If we integrate (2.13) over all space that lies above the horizontal plane $z = \ell \gg \delta$, then we obtain

$$\frac{d}{dt} \int \mathbf{u} \cdot \boldsymbol{\omega} dV = -\oint_S \mathbf{F} \cdot d\mathbf{S} \approx -2\Omega \int_{z=\ell} \mathbf{u}^2 dA. \quad (2.17a)$$

Similarly, integrating (2.13) over all space that lies below the horizontal plane $z = -\ell$ yields

$$\frac{d}{dt} \int \mathbf{u} \cdot \boldsymbol{\omega} dV = -\oint_S \mathbf{F} \cdot d\mathbf{S} \approx 2\Omega \int_{z=-\ell} \mathbf{u}^2 dA. \quad (2.17b)$$

So we obtain negative helicity above the source and positive helicity below, as expected from an analysis of monochromatic waves.

More generally, if we are remote from all sources of buoyancy, and we consider only the helicity transported by the fast, low-frequency waves, we may integrate (2.16) over a cylindrical control volume V_R to give

$$\frac{d}{dt} \int_{V_R} \mathbf{u} \cdot \boldsymbol{\omega} dV = 2\Omega \left\{ \int_{S_T} \mathbf{u}^2 dA - \int_{S_B} \mathbf{u}^2 dA \right\}, \quad (2.18)$$

where S_T is the top of the cylindrical control volume and S_B the bottom. Evidently, the growth of helicity in V_R due to the flux of low-frequency inertial waves depends on only the difference in kinetic energy between the top and bottom of V_R . In particular, inertial waves carry helicity from regions of high kinetic energy to regions of low kinetic energy.

2.4 The Source Term in the Helicity Equation.

Since the buoyancy field can be considered as quasi-static at low Ro , the source term $\mathcal{G}\mathbf{g}$ in the linear equation (2.3) is effectively prescribed and independent of the wave dynamics. We therefore have a source of waves of unambiguous magnitude and distribution. However, this is not the case with the helicity equation (2.13) because of the appearance of \mathbf{u} in the source term S_h , and so some caution must be exercised when discussing this source term. In fact, we shall see that, during the dispersion of waves from a localised distribution of buoyancy, the velocity field automatically adjusts the local sign of S_h so that, on average, the upper regions of a buoyant cloud develop a negative sign in S_h , while the lower regions develop a positive sign. In short, the local value of S_h automatically adjusts to be of the same sign as the helicity emanating from the buoyant cloud in the form of inertial waves.

We can gain some insight into this process by supposing that, once again, the buoyancy source is localised near the plane $z = 0$, say confined to the region $-\delta < z < \delta$. Consider, for example, the first contribution to (2.15), $S_1 = \nabla \cdot (\mathbf{u} \times (\mathcal{G}\mathbf{g}))$. If we integrate this over the top half of the buoyancy field, $z > 0$, we obtain

$$\Omega \int_{z>0} S_1 dV = \Omega \int_{z=0} \mathbf{u} \times (\mathcal{G}\mathbf{g}) \cdot d\mathbf{S} = \int_{z=0} (\mathcal{G}\mathbf{g}) \cdot (\mathbf{u} \times \boldsymbol{\Omega}) dA. \quad (2.19)$$

However, from (2.1) we expect the approximate force balance $2\mathbf{u} \times \boldsymbol{\Omega} \approx \nabla(p/\rho) - \mathcal{G}\mathbf{g}$ in low-frequency waves, and so we find

$$2\Omega \int_{z>0} S_1 dV \approx - \int_{z=0} (\mathcal{G}\mathbf{g})^2 dA + \int_{z=0} \mathcal{G}\mathbf{g} \cdot \nabla(p/\rho) dA. \quad (2.20)$$

Similarly

$$2\Omega \int_{z<0} S_1 dV \approx \int_{z=0} (\mathcal{G}\mathbf{g})^2 dA - \int_{z=0} \mathcal{G}\mathbf{g} \cdot \nabla(p/\rho) dA, \quad (2.21)$$

and so, pressure terms apart, S_1 integrates over the top or bottom half of the cloud to have the same sign as the helicity locally emanating from the cloud in the form of inertial waves. Of course, we must add to this the contribution from S_2 , which turns out to be more complicated. Nevertheless, we shall see that, *on average*, S_h near the

edges of a buoyant cloud does indeed take the same sign as the helicity associated with local inertial waves leaving the cloud.

We shall now illustrate this by considering first a simple Gaussian distribution of \mathcal{G} located at the origin, reminiscent of the studies detailed in Loper (2001) and Shimizu & Loper (2000). We then consider a random field of buoyancy confined to the layer $-\ell < z < \ell$.

3. The Dispersal of Helicity from a Single Buoyant Blob at Low Ro

Consider the case where $\mathbf{g} = -g\hat{\mathbf{e}}_y$ and

$$\mathcal{G} = -\mathcal{G}_0 \exp\left(-\frac{(x^2 + y^2)}{\delta^2}\right) \exp\left(-\frac{z^2}{(\alpha\delta)^2}\right). \quad (3.1)$$

The wave dispersion pattern associated with such a Gaussian blob is discussed in Davidson (2014). The first point to notice is that the dispersion pattern is dominated by low-frequency waves propagating along the rotation axis above and below the blob, in the sense that the radiation density is highest within an imaginary cylinder which is aligned with $\mathbf{\Omega}$ and circumscribes the buoyant anomaly. To understand why the radiation density is highest in this cylindrical region we must recall that the group velocity of inertial waves is perpendicular to \mathbf{k} . Thus the energy associated with all horizontal wave-vectors radiates along the rotation axis, and so all the energy contained within a thin horizontal disc in \mathbf{k} -space propagates along a narrow cylinder in real space. On the other hand, only one orientation of \mathbf{k} will transport energy to a particular location remote from the cylinder that circumscribes the buoyant anomaly. The process of channelling energy from a two-dimensional object in \mathbf{k} -space (a disk) to a one-dimensional object in real space (the tangent cylinder which circumscribes the blob) amplifies the radiation density on the rotation axis (Davidson, 2013). In short, the dispersion pattern is dominated by columnar vortices (transient Taylor columns) composed of low-frequency waves which propagate along the rotation axis.

To obtain the dispersion pattern within this tangent cylinder, we invoked the idea of *vertical jump conditions* across the buoyant blob after the initial passage of inertial waves. This rests on the fact that the waves within the tangent cylinder are of low frequency, and so time dependence is significant only near the advancing front of the columnar wave packets. Near the blob, on the other hand, equation (2.4) and its curl gives us

$$2\mathbf{\Omega} \cdot \nabla \mathbf{u} + \nabla \mathcal{G} \times \mathbf{g} \approx 0, \quad (3.2)$$

$$2\boldsymbol{\Omega} \cdot \nabla \boldsymbol{\omega} \approx \mathbf{g} \nabla^2 \mathcal{G} - (\mathbf{g} \cdot \nabla) \nabla \mathcal{G}. \quad (3.3)$$

Integrating vertically through the blob yields the jump conditions (Davidson, 2014)

$$\Delta u_x \approx \Delta u_y \approx 0,$$

$$\Delta u_z \approx \frac{g}{2\Omega} \int (\partial \mathcal{G} / \partial x) dz, \quad (3.4)$$

and

$$\Delta \omega_z \approx 0. \quad (3.5)$$

From (3.5) we see that a cyclonic (or anticyclonic) columnar vortex which forms above the blob must correspond to a cyclonic (or anticyclonic) vortex below the blob. Moreover, for the Gaussian profile (3.1) we have $\Delta u_z > 0$ for $x > 0$ and $\Delta u_z < 0$ for $x < 0$. Given that u_z is antisymmetric about the plane $z = 0$, we conclude that u_z diverges from the blob for $x > 0$ and converges onto the buoyant anomaly for $x < 0$. Finally, noting that upward propagating inertial waves carry negative helicity and downward propagating waves positive helicity, we conclude that the dispersion pattern within the tangent cylinder consists of a cyclone-anticyclone pair of columnar vortices above the blob matched to a cyclone-anticyclone pair below. Moreover, the cyclonic wave packets above and below the blob are confined to $x < 0$ and the anticyclones to $x > 0$.

This is illustrated in Figures 3 and 4 using the results of direct numerical simulations of the full Navier-Stokes equation, including the nonlinear and viscous forces. The Courant condition is based on the group velocity of inertial waves and the buoyancy field, \mathcal{G} , is advected by an advection-diffusion equation, with a diffusivity κ equal to that of the viscosity. The simulations were performed in a 512^3 periodic domain using the pseudo-spectral code described in Yeung & Zhou (1998) and Ranjan & Davidson (2014). Because the boundary conditions are periodic, the simulations were halted before waves reached the upper and lower boundaries. Figure 3 shows the results for the case of $\text{Ro} = \mathcal{G}_0 g / 2\Omega^2 \delta = 0.01$, an Ekman number of $\text{Ek} = \nu / \Omega \delta^2 = 0.029$, $\alpha = 2$ and time $\Omega t = 8$, while Figure 4 gives the results for the same values of Ro , Ek and Ωt , but for $\alpha = 1/2$. Note that the vertical jump conditions are indeed satisfied in both cases and that the dispersion pattern is as expected.

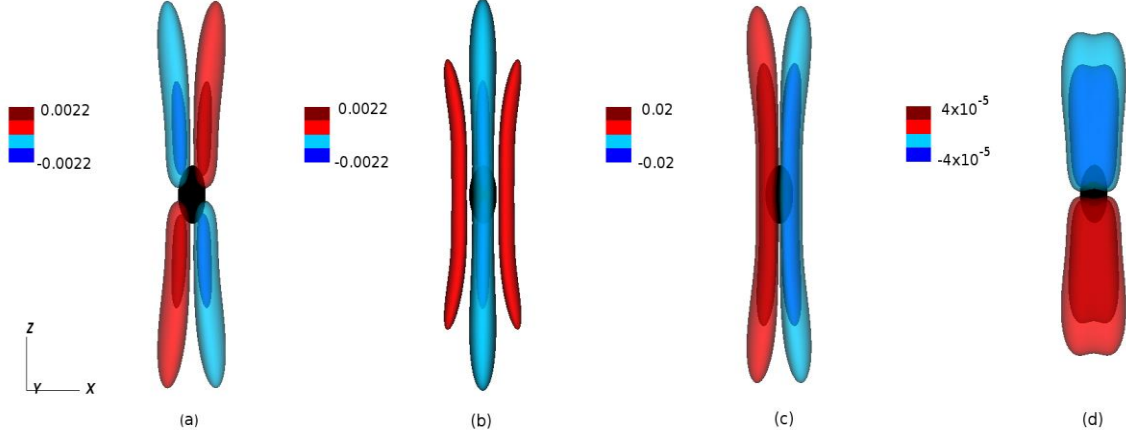


Figure 3. The dispersion pattern from a Gaussian blob for the case of $Ro = 0.01$, $\alpha = 2$ and time $\Omega t = 8$. Contours of energy coloured by (a) u_z , (b) u_y , (c) ω_z and (d) h .

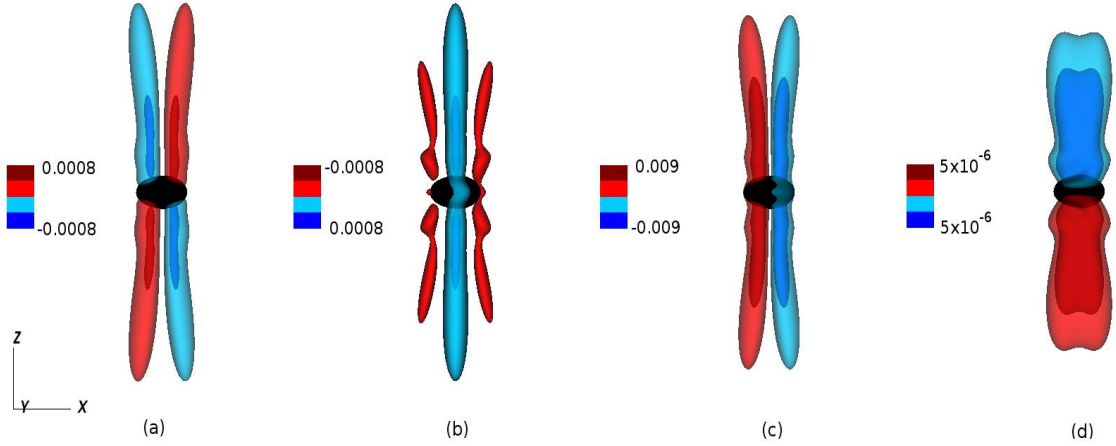


Figure 4. The dispersion pattern from a Gaussian blob for the case of $Ro = 0.01$, $\alpha = 1/2$ and $\Omega t = 8$. Contours of energy coloured by (a) u_z , (b) u_y , (c) ω_z and (d) h .

The distribution of h on the z axis is shown for different times in Figure 5. It is clear that, after a time of $\Omega t \approx 6$, the magnitude of h just above and below the buoyant anomaly saturates. This can be understood from the fact that the source S_h is linear in \mathbf{u} whereas the flux is quadratic in the velocity. As the magnitude of \mathbf{u} , and hence h , increases there comes a point at which the flux of helicity equals the rate of generation of helicity within the buoyant blob, which occurs when $u \sim \mathcal{G}g/\Omega$. After this, the peak in h is fixed and helicity simply spreads out along the rotation axis at the group velocity of low-frequency inertial waves, $\mathbf{c}_g = \pm 2\Omega/k$.

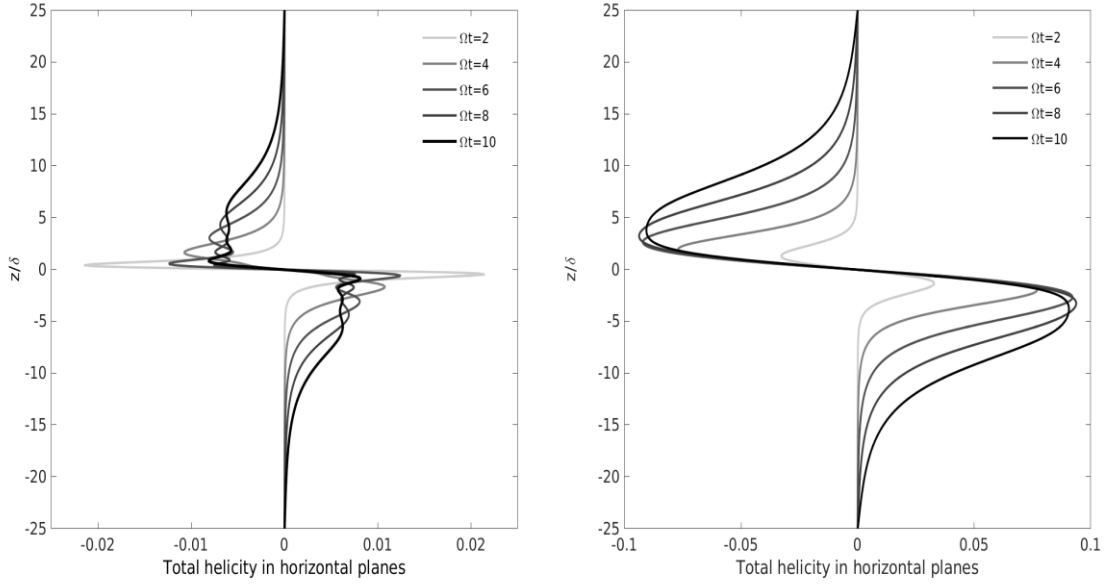


Figure 5. The distribution of h on the z axis is shown for different times corresponding to the cases shown in Figures 3 and 4. (a) $\alpha = 1/2$, (b) $\alpha = 2$.

Of particular interest is the distribution of the source term $S_h = S_1 + S_2$ within the buoyant anomaly, which is shown in Figures 6 and 7. In both cases the contribution from $S_1 = \nabla \cdot (\mathbf{u} \times (\mathcal{G}\mathbf{g}))$ is predominantly negative for $z > 0$ and positive for $z < 0$, as suggested by (2.20) and (2.21), whereas $S_2 = 2\mathbf{g} \cdot (\mathbf{u} \times \nabla \mathcal{G})$ is often of the opposite sign. In particular, while the contribution to S_2 associated with $-gu_z \partial \mathcal{G} / \partial x$ has the same sign as S_h , that associated with $gu_x \partial \mathcal{G} / \partial z$ does not. However, when all the terms are added to give S_h , we see that in both cases the source term is uniformly negative in the top half of the blob and positive in the lower half. Moreover, in Figure 8 we show the horizontal averages of S_h , h and $\partial h / \partial t$ as a function of z for the case of $\alpha = 2$ at $\Omega t = 8$. While S_h and h are well correlated, at least within the buoyant blob, there is no such strong spatial correlation between S_h and $\partial h / \partial t$. This is consistent with what is observed in the numerical dynamo, as discussed in §1.

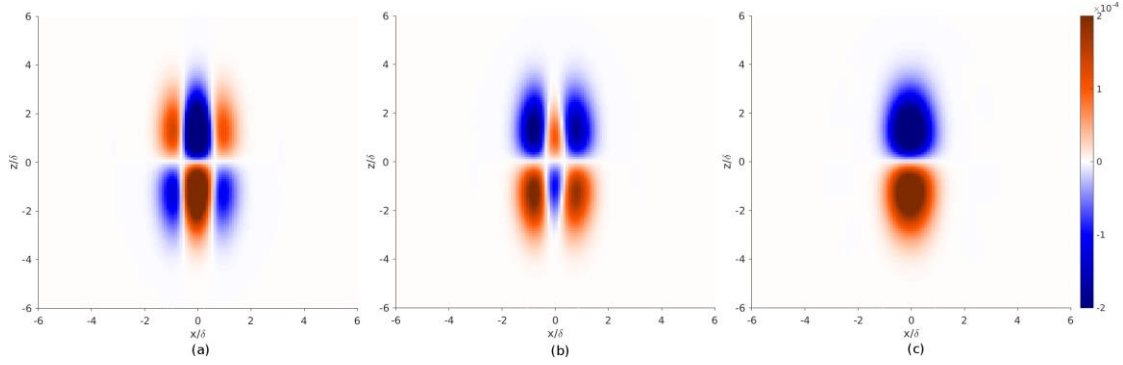


Figure 6. The distribution of the helicity source terms S_1 , S_2 and $S_h = S_1 + S_2$ for a Gaussian blob for the case of $Ro = 0.01$, $\alpha = 2$ and time $\Omega t = 8$.

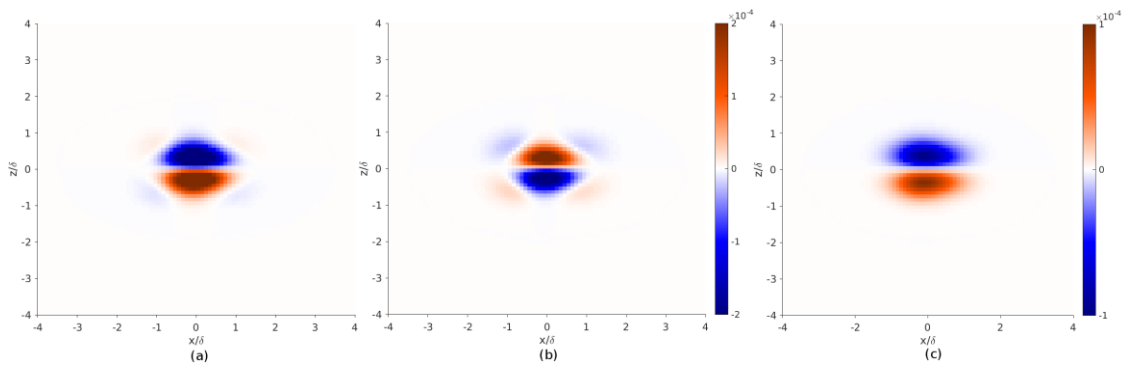


Figure 7. The distribution of the helicity source terms S_1 , S_2 and $S_h = S_1 + S_2$ for a Gaussian blob for the case of $Ro = 0.01$, $\alpha = 1/2$ and time $\Omega t = 8$.

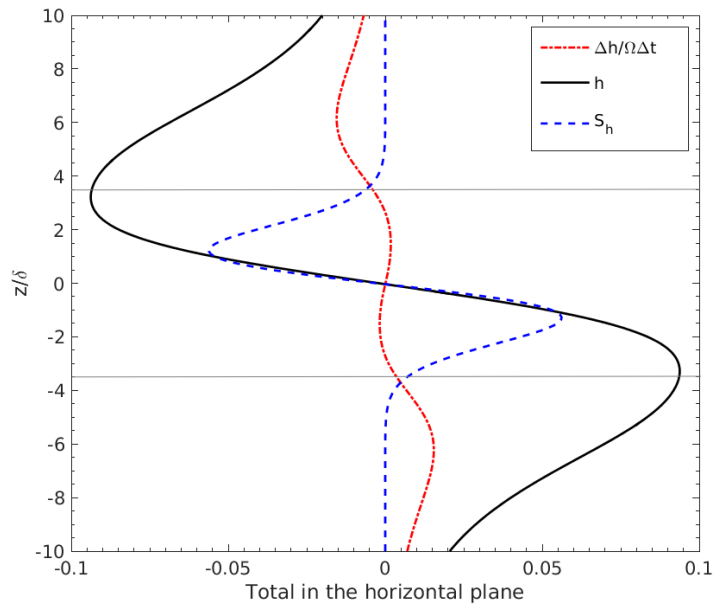


Figure 8. The horizontal averages of S_h , h and $\partial h / \partial t$ as a function of z for the case of $Ro = 0.01$, $\alpha = 2$ and $\Omega t = 8$. The horizontal lines indicate the extent of the blob.

We can understand this behaviour using (2.13). To focus thoughts, consider the half-space $z > 0$. Let us divide the dispersion pattern into three regions, a lower region, V_{source} , in the vicinity of the buoyant blob, an upper region, V_{front} , which includes the advancing wave front, and the region in between, V_{flux} . Recalling that we are dealing with low-frequency waves, time dependence is significant only in V_{front} . So the helicity equation in these three regions takes the form

$$V_{\text{front}} : \quad \frac{\partial}{\partial t} (\mathbf{u} \cdot \boldsymbol{\omega}) \approx -\nabla \cdot \mathbf{F}, \quad (3.6)$$

$$V_{\text{flux}} : \quad \nabla \cdot \mathbf{F} \approx 0, \quad (3.7)$$

$$V_{\text{source}} : \quad \nabla \cdot \mathbf{F} \approx S_h, \quad (3.8)$$

Expression (3.6) then tells us that the advancing front, which has $h < 0$, must be fed by an upward flux of negative helicity, while (3.7) tells us that this same negative flux must emerge from the source region lower down. Finally, (3.8) tells us that this upward flux of negative helicity must be generated by the integral of S_h over the upper half of the buoyant blob. In short, the integral of S_h over $z > 0$ must be negative in order to feed the negative helicity in the advancing front higher up. Clearly, a similar argument applied to $z < 0$ tells us that the integral of S_h over the lower half of the blob must be positive.

Finally, before leaving the Gaussian blob, we note that a simple analysis of the advancing front explains why upward (downward) propagating wave-packets carry negative (positive) helicity. Consider the region V_{front} above the blob where, viscous forces apart, (2.4) gives,

$$\frac{\partial \boldsymbol{\omega}}{\partial t} = 2\boldsymbol{\Omega} \cdot \nabla \mathbf{u}. \quad (3.9)$$

We now move into a frame of reference moving with the dominant group velocity of the upward propagating wave packet. In such a frame of reference the front will look approximately steady, and so (3.9) becomes

$$c_g \frac{\partial \boldsymbol{\omega}}{\partial z} = (2\boldsymbol{\Omega}/k_d) \frac{\partial \boldsymbol{\omega}}{\partial z} \approx -2\boldsymbol{\Omega} \cdot \nabla \mathbf{u}, \quad (3.10)$$

where k_d is the dominant wavenumber. It follows that, near the front, we have $\boldsymbol{\omega} \approx -k_d \mathbf{u}$ and hence $h \approx -k_d \mathbf{u}^2$. Clearly, a similar argument applied to the downward propagating front yields $h \approx k_d \mathbf{u}^2$. We believe that this is the first time a simple physical explanation has been given for the asymmetry in the sign of h associated with inertial waves dispersing from a localized source.

4. The Dispersal of Helicity from a Random Layer of Buoyancy

4.1 Low Rossby Number

Let us now consider the dispersion of helicity from a random layer of buoyancy. Once again, we show the results of direct numerical simulations of the full Navier-Stokes equation corresponding to $\boldsymbol{\Omega} = \Omega \hat{\mathbf{e}}_z$ and $\mathbf{g} = -g \hat{\mathbf{e}}_y$. As before, \mathcal{G} is advected by an advection-diffusion equation, with a diffusivity κ equal to that of the kinematic viscosity. This time, however, we use an elongated periodic domain of $512 \times 512 \times 1536$ modes. Our initial condition consists of 2000 randomly located density perturbations which are restricted to a horizontal slab located at the mid-height of the triply periodic domain. Each of the density perturbations is of the form $\mathcal{G}_i = -\mathcal{G}_0 \exp[-(\mathbf{x} - \mathbf{x}_i)^2 / \delta_i^2]$, where \mathbf{x}_i locates the center of the blob and the length-scales δ_i are chosen uniformly from the range $\delta/2 \leq \delta_i \leq 2\delta$. The centers \mathbf{x}_i are restricted to a horizontal layer $-2.8\delta < z < 2.8\delta$ which fills the computational domain in the x and y directions. The size of the computational domain is $50\delta \times 50\delta \times 150\delta$.

In Figures 9–12, the Rossby number is set to $\text{Ro} = \mathcal{G}_0 g / 2\Omega^2 \delta = 0.01$, the Ekman number is $\text{Ek} = \nu / \Omega \delta^2 = 0.0023$ and time is $\Omega t = 12$. Figure 9 shows snapshots of $-\mathcal{G}$, u_z and h in the x - z plane, and as expected we see wave-packets in the form of cyclone-anticyclone pairs emerging from the buoyant cloud, carrying negative helicity upward and positive helicity downward. The corresponding helicity source terms, S_1 , S_2 and $S_h = S_1 + S_2$, averaged in y , are shown in Figure 10, again in the x - z plane. As with a single buoyant blob, the spatially averaged values of S_h take the same sign as the local value of h , being predominantly negative in the upper half of the buoyancy field and positive in the lower half. This distribution of S_h is an inevitable consequence of (3.6)–(3.8).

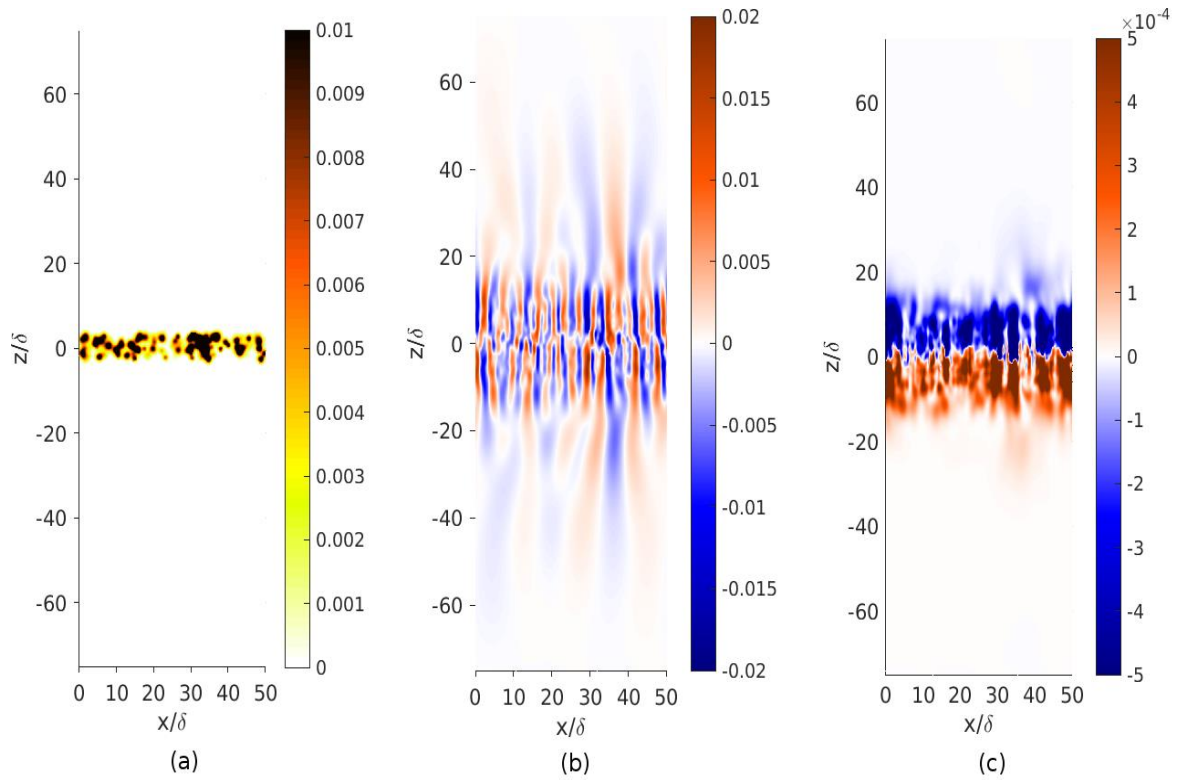


Figure 9. A horizontal layer of buoyant blobs provides the initial condition for a simulation with $Ro = 0.01$ and $Ek = 0.0023$. (a) the buoyancy field, $-\mathcal{G}$, (b) u_z , and (c) h , all in the x - z plane at time $\Omega t = 12$.

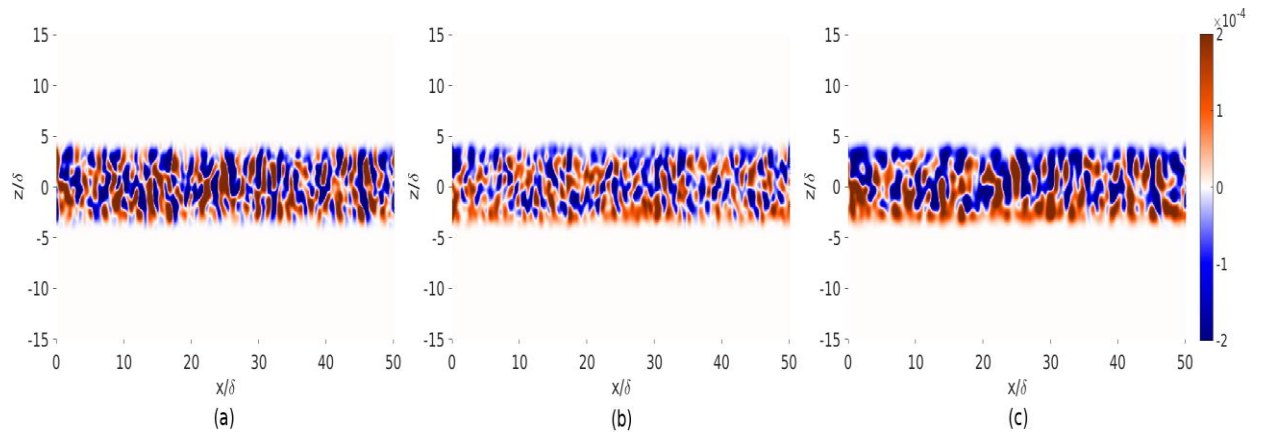


Figure 10. Helicity sources in a horizontal layer of buoyant blobs: (a) S_1 , (b) S_2 and (c) $S_h = S_1 + S_2$, all averaged in y and all shown in the x - z plane. $Ro = 0.01$, $Ek = 0.0023$ and $\Omega t = 12$.

The corresponding horizontally averaged values of h , $\partial h/\partial t$ and S_h are shown in Figure 11 as a function of z , with $-40 < z/\delta < 40$ and $\partial h/\partial t$ estimated as $\Delta h/\Delta t$. This shows the evolution of h , $\partial h/\partial t$ and S_h over a range of times, $\Omega t = 4 \rightarrow 20$. As with the Gaussian blob, the magnitude of the helicity at the top and bottom of the cloud eventually saturates. Also, as the helicity propagates away from the cloud at the group velocity of low-frequency inertial waves, the spatial extent of the source remains more or less constant, which is a consequence of the low value of Ro . (At low Ro there is very little advection of the buoyancy field.) Finally note that, while h is well correlated with S_h within the buoyant slab, there is no corresponding correlation between $\partial h/\partial t$ and S_h at large times, consistent with what we observed for a single buoyant blob.

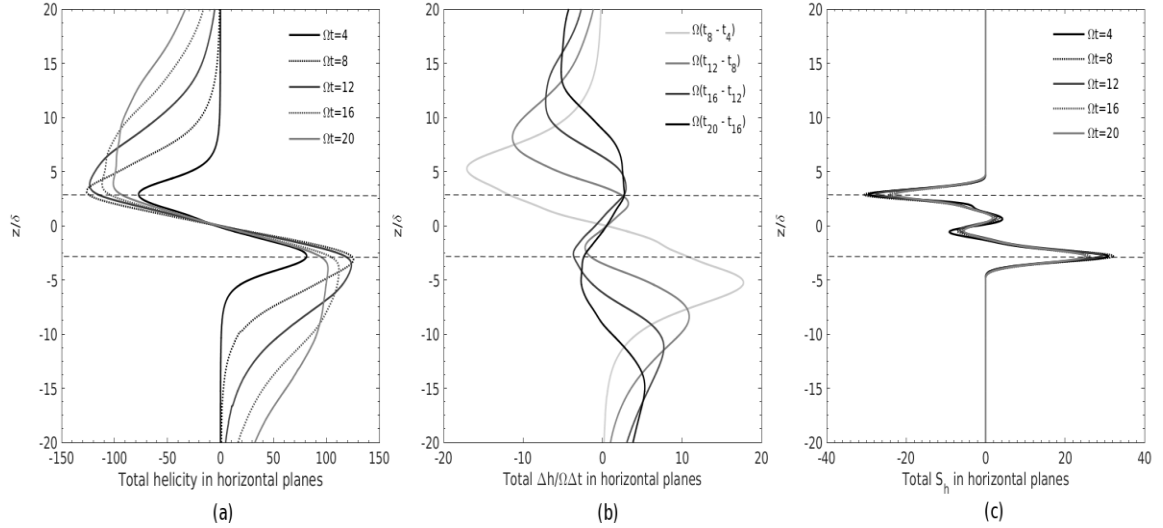


Figure 11. The evolution of the horizontally averaged values of h , $\partial h/\partial t$ and S_h for $Ro = 0.01$, $Ek = 0.0023$ and $\Omega t = 4 \rightarrow 20$.

Finally, Figure 12 shows the corresponding spatial distributions of $-\mathcal{G}$ (top), helicity (middle), and helicity source, S_h (bottom), in the three horizontal planes $z/\delta = -2.8, 0, 2.8$. While the detailed distributions of h and S_h are highly intermittent, the statistically asymmetric distribution about $z = 0$ is clear.

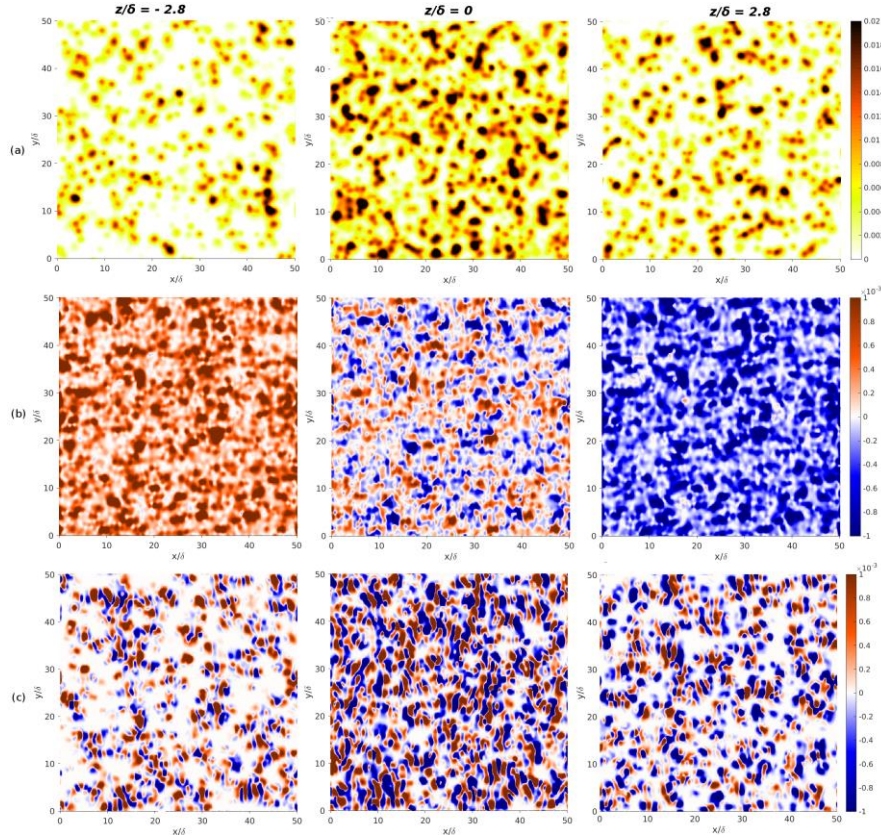


Figure 12. The buoyancy field, $-\mathcal{G}$ (top), helicity (middle), and helicity source, S_h (bottom), for a layer of buoyant blobs, each viewed in the horizontal planes, $z/\delta = -2.8, 0, 2.8$. $Ro = 0.01$, $Ek = 0.0023$ and $\Omega t = 12$.

4.2 Rossby Number of Order Unity

In some planetary dynamo simulations the value of Ro corresponding to the small-scale structures is not that much less than unity, perhaps $Ro \sim 0.1$. In order to determine the sensitivity of our results to Ro , we now consider a case in which Ro is of order unity. Figures 13→16 show the results where the initial Rossby number is set to $Ro = \mathcal{G}_0 g / 2\Omega^2 \delta = 1$. All other parameters remain unchanged. Figure 13 shows snapshots of (a) $-\mathcal{G}$, (b) u_z and (c) h , all at $\Omega t = 12$ and all in the x - z plane. Rather remarkably, despite the much higher value of Ro , the wave field looks very similar to the low- Ro case. The main difference between Figures 9 and 13 is that there is now significant advection of the buoyancy by the wave field, which causes some mixing of \mathcal{G} . This, in turn, causes the characteristic transverse length-scale to increase as a result of cross-diffusion of the buoyancy field, growing by a factor of ~ 3 by $\Omega t = 12$. The growth in this length-scale results in the effective value of Ro falling from unity at $t = 0$ to ~ 0.3 at $\Omega t = 12$.

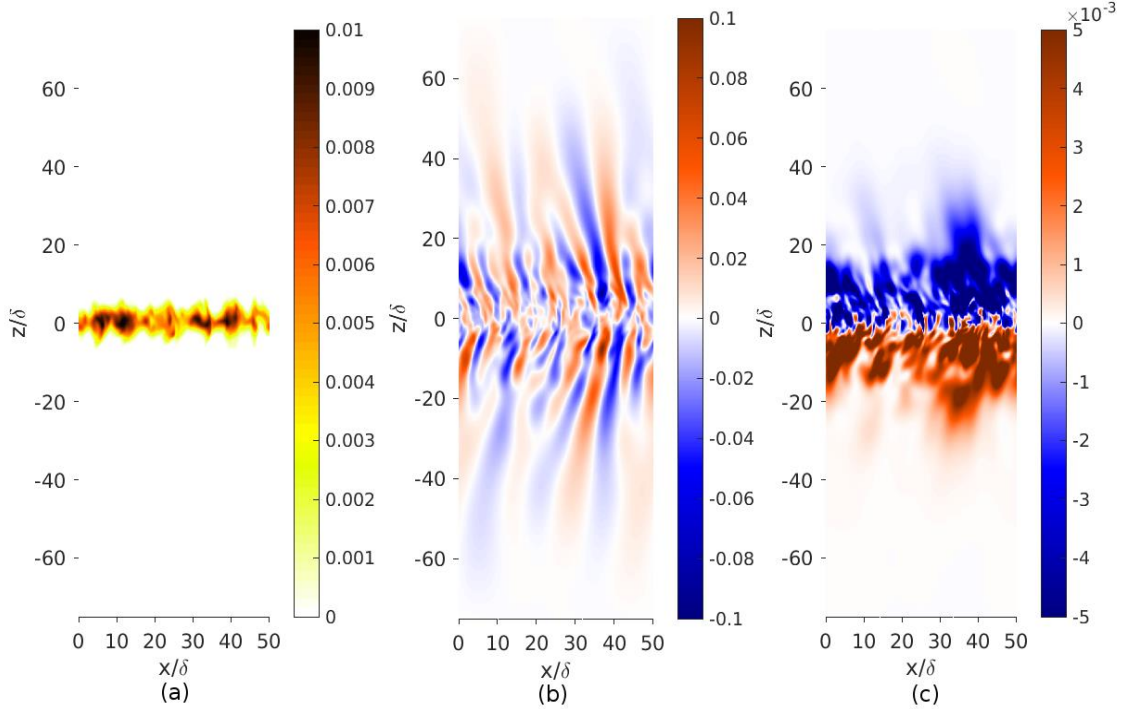


Figure 13. A horizontal layer of buoyant blobs provides the initial condition for a simulation with $Ro = 1$ and $Ek = 0.0023$. (a) the buoyancy field $-\mathcal{G}$, (b) u_z , and (c) h , all in the x - z plane and at time $\Omega t = 12$.

The horizontal movement of the \mathcal{G} -field leads to the observed inclination of the columnar eddies which, in principle, is similar to the trailing Taylor columns observed by Hide, Ibbetson and Lighthill (1968). The corresponding distributions of the helicity source terms, S_1 , S_2 and $S_h = S_1 + S_2$, averaged in y , are shown in Figure 14, again in the x - z plane and for $\Omega t = 12$. In this case all three source terms are predominantly negative at the top of the buoyant cloud and positive at the bottom. There is also a marked oscillation in S_2 , though not in S_h , which is less evident (though still detectable) in the low- Ro case.

The horizontally averaged values of h , $\partial h / \partial t$ and S_h are shown in Figure 15 as a function of z , with $-40 < z / \delta < 40$. This shows the evolution of h , $\partial h / \partial t$ and S_h over a range of times, $\Omega t = 4 \rightarrow 20$. Unlike the low- Ro case, the magnitude of the helicity at the top and bottom of the cloud does not saturate, almost certainly because the r.m.s. buoyancy field declines throughout the simulation as a result of the mixing-induced cross diffusion of \mathcal{G} . Nevertheless, we see the usual spatial correlation in the signs of the horizontally averaged values of h and S_h .

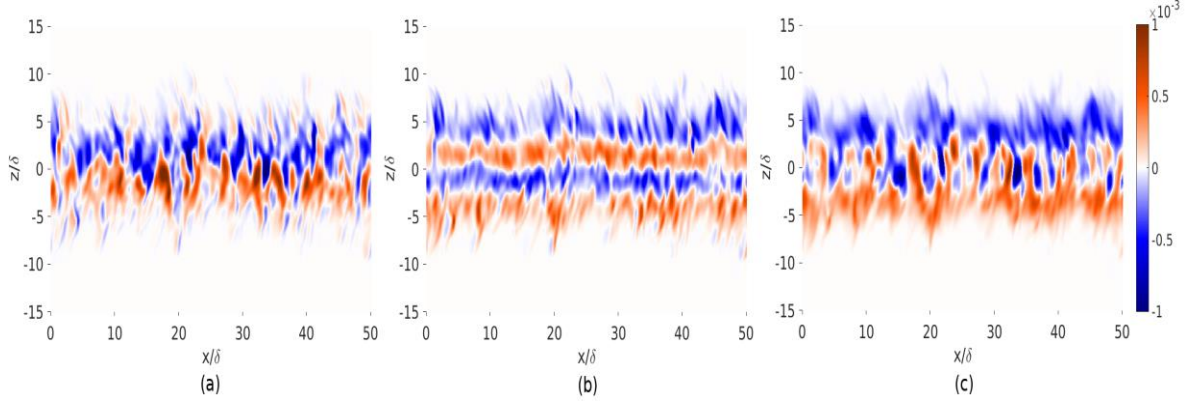


Figure 14. The helicity sources in a horizontal layer of buoyant blobs: (a) S_1 , (b) S_2 , and (c) $S_h = S_1 + S_2$, all averaged in y and shown in the x - z plane. $Ro = 1$, $Ek = 0.0023$ and $\Omega t = 12$.

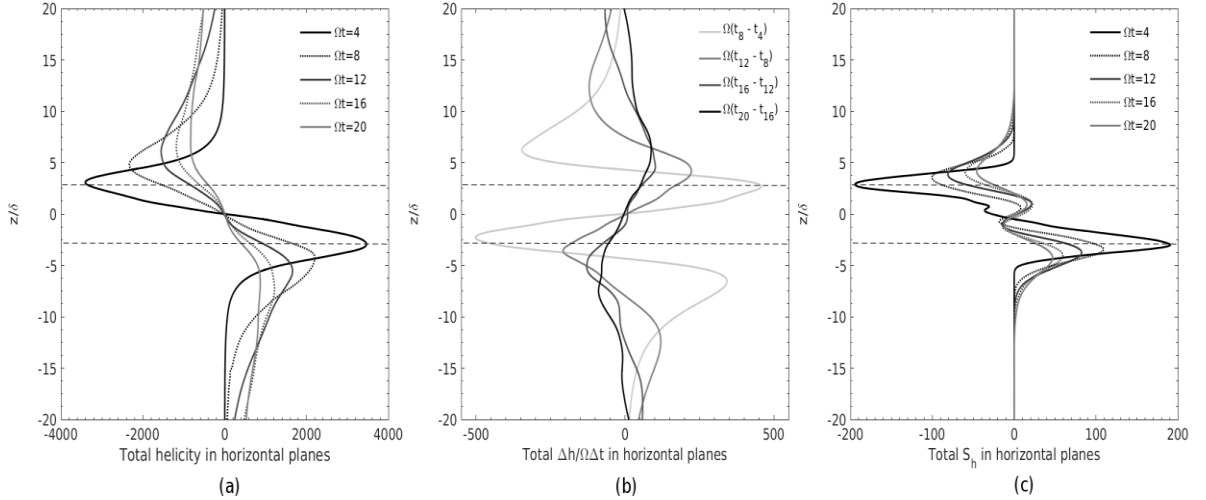


Figure 15. The evolution of the horizontally averaged values of h , $\partial h / \partial t$ and S_h for $Ro = 1$, $Ek = 0.0023$, $\Omega t = 4 \rightarrow 20$.

Finally, Figure 16 shows the distribution of $-\mathcal{G}$ (top), helicity (middle), and helicity source, S_h (bottom), in the three horizontal planes $z/\delta = -2.8, 0, 2.8$. As in Figure 12, the distributions of h and S_h are complicated, but the statistically asymmetric distribution about $z = 0$ is clear. The main effect of increasing Ro is that the \mathcal{G} field is smoother (less spotty) and has a larger transverse length-scale, almost certainly as a result of the mixing of the buoyancy by the wave-induced velocity field, and by the enhanced diffusion that ensues. It is also notable that there is now significant anisotropy in the x - y plane, with S_h adopting a streaky structure with the streaks aligned with \mathbf{g} .

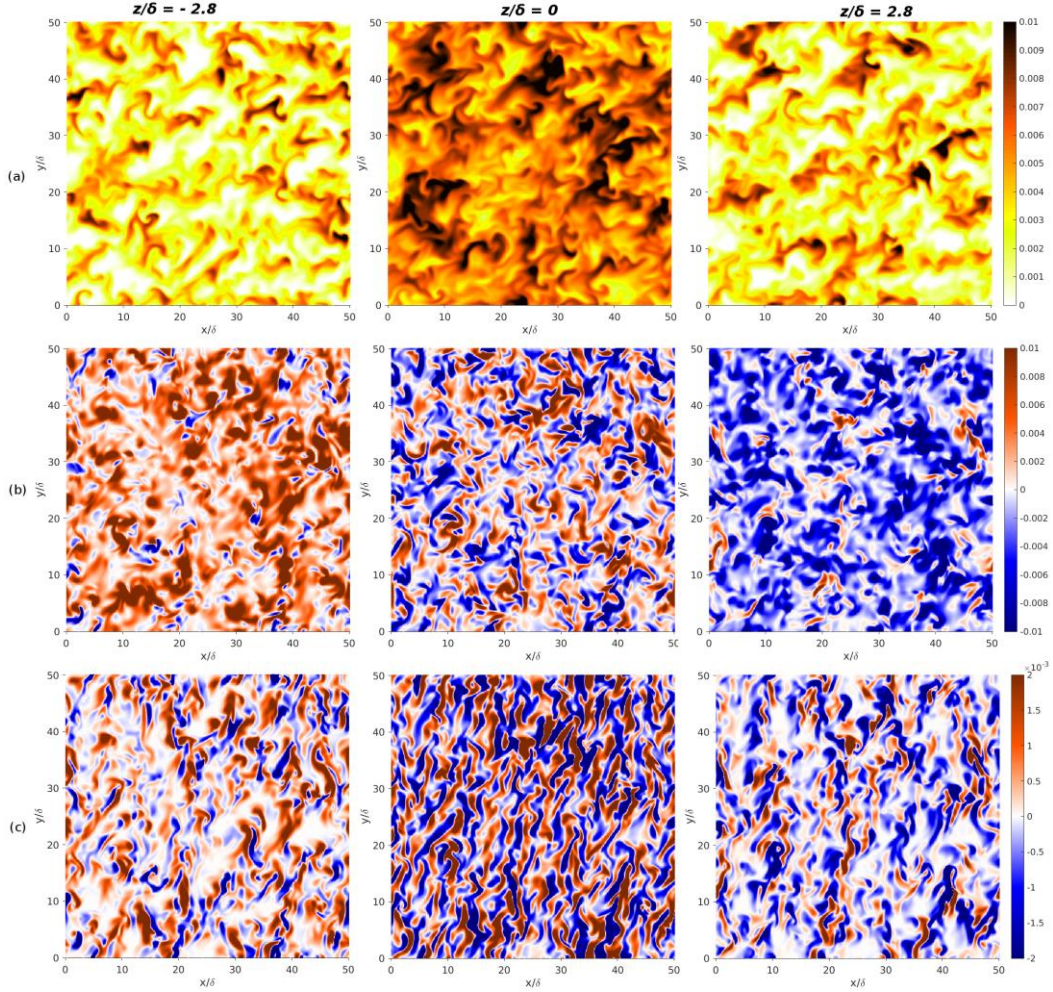


Figure 16. The buoyancy field, $-\mathcal{G}$ (top), helicity (middle), and helicity source, S_h (bottom), for a layer of buoyant blobs, each viewed in the horizontal planes $z/\delta = -2.8, 0, 2.8$. $Ro = 1$, $Ek = 0.0023$ and $\Omega t = 12$.

5. Discussion: Implications for Numerical Dynamos and Planetary Cores

So far we have ignored the presence of boundaries, which are of course important for the dynamics in a planetary core. The first point to note is that low-frequency inertial wave packets travelling along the rotation axis will reflect at the mantle, reversing their group velocity and helicity in the process (Greenspan, 1968). In the absence of dissipation, this produces standing waves, which are of course Taylor columns. The helicity in a Taylor column is zero, and so the mechanism of helicity segregation described here will be effective in a planetary core only if there is significant dissipation. That is to say, in order to avoid the perfect cancelation of helicity in the reflected and incident waves, we require that waves launched in the interior be somewhat dissipated before they reach the mantle. Since the Ekman number is tiny in

the core of the earth, this dissipation can only be Ohmic in nature. In principle, the magnitude of the Ohmic dissipation can be estimated, but the calculation is very sensitive to the assumed magnitude of the magnetic field, which is a poorly constrained parameter, and to the size of the smallest scales in the core, which is unknown. So the question of dissipation remains an open one.

A second difficulty arises from the fact that, although the simulations exhibit a statistical bias in the concentration of buoyant anomalies towards the equatorial regions, in practice the fluctuations in density are everywhere. So buoyant anomalies which are closer to the mantle than the equator will emit waves whose helicity in the interior is opposite in sign to that of the waves which were launched close to the equator. Once again, there will be a tendency for cancellation in helicity, and so the segregation mechanism proposed here will be effective only if the statistical inhomogeneity in buoyancy sources is strong enough.

A third weakness of the inertial-wave model for establishing planetary helicity distributions is that the magnetic field within a planet will modify the inertial waves, forming hybrid magnetic-Coriolis waves. This process is discussed in, for example, Bardsley & Davidson (2016, 2017), where it is noted that the main effect of the magnetic field is to reduce the magnitude of the group velocity. However, such hybrid waves still carry negative helicity northward and positive helicity to the south, just like inertial waves.

Given the three caveats above, perhaps the strongest argument in favour of helicity segregation by inertial waves is the simplicity of (2.18). Perhaps it is worth taking a closer look at this equation. Rearranging the terms in the inviscid helicity equation (2.10), we find that, without approximation,

$$\frac{\partial}{\partial t}(\mathbf{u} \cdot \boldsymbol{\omega}) = -\nabla \cdot \mathbf{F} + S_2, \quad \mathbf{F} = -(2\mathbf{u}^2)\boldsymbol{\Omega} - \mathbf{u} \times \frac{\partial \mathbf{u}}{\partial t}. \quad (5.1)$$

Now

$$\mathbf{u} \times \frac{\partial \mathbf{u}}{\partial t} < 2\Omega \mathbf{u}^2,$$

since the highest frequency for inertial waves is 2Ω . It follows that $\mathbf{F} = -(2\mathbf{u}^2)\boldsymbol{\Omega}$ is always the larger of the two contributions to the wave flux. Moreover

$$\nabla \cdot \left(\mathbf{u} \times \frac{\partial \mathbf{u}}{\partial t} \right) = \boldsymbol{\omega} \cdot \frac{\partial \mathbf{u}}{\partial t} - \mathbf{u} \cdot \frac{\partial \boldsymbol{\omega}}{\partial t}, \quad (5.2)$$

and so we may drop the term $\mathbf{u} \times \partial \mathbf{u} / \partial t$ all together in one of two situations:

- (i) the helicity is being carried by low-frequency wave packets, $\varpi \ll |\boldsymbol{\Omega}|$, as in equation (2.18);
- (ii) we have maximal helicity in the waves, with the velocity and vorticity fields proportional, $\boldsymbol{\omega} = \mp k \mathbf{u}$, as in a monochromatic inertial wave and as observed in inertial wave-packets by Davidson & Ranjan (2015).

In either of these situations we have the approximation

$$\frac{\partial}{\partial t} (\mathbf{u} \cdot \boldsymbol{\omega}) \approx \nabla \cdot \left[(2\mathbf{u}^2) \boldsymbol{\Omega} \right] + 2\mathbf{g} \cdot (\mathbf{u} \times \nabla \vartheta). \quad (5.3)$$

Let us integrate this over a cylindrical annulus, V_N , lying outside the tangent cylinder, of radial extent Δs , and bounded above by the mantle and below by the equator

$$\frac{d}{dt} \int_{V_N} \mathbf{u} \cdot \boldsymbol{\omega} dV = -2\Omega \left\{ \int_{equator} \mathbf{u}^2 dA - \int_{mantle} \mathbf{u}^2 dA \right\} + \int_{V_N} S_2 dV, \quad (5.4)$$

Similarly, for the corresponding annulus in the south, V_S , which is bounded below by the mantle and above by the equator, we have

$$\frac{d}{dt} \int_{V_S} \mathbf{u} \cdot \boldsymbol{\omega} dV = 2\Omega \left\{ \int_{equator} \mathbf{u}^2 dA - \int_{mantle} \mathbf{u}^2 dA \right\} + \int_{V_S} S_2 dV, \quad (5.5)$$

where \mathbf{u} in (5.4) and (5.5) is the fluctuating velocity. Now it is difficult predict what the integral of S_2 will be, as can be seen by comparing Figures 10(b) and 14(b). Moreover, we have omitted all dissipative and magnetic effects in these equations. Nevertheless, it seems that a relatively large fluctuating kinetic energy in the equatorial regions will favor the north-south asymmetry in the azimuthally-averaged helicity shown in Figure 1(c) and 2(a), and this applies to inertial waves of all frequencies. Of course, physically this reflects the fact that, if we have more wave activity near the equator than the mantle, then waves will tend to disperse away from the equatorial regions, carrying with them helicity of the observed signs.

6. Conclusions

The strong spatial correlation between the distribution of h and of S_h in the dynamo simulations tends to suggest an *in situ* generation of helicity in dynamo simulations, rather than the dispersal of helicity by waves, as previously argued by the authors. However, the observation that there is no such correlation between $\partial h/\partial t$ and S_h argues against such an in situ generation mechanism. Either way, the correlation, or lack of correlation, between h , $\partial h/\partial t$ and S_h needs to be explained.

We have offered an explanation for the paradoxical observation that h and S_h are strongly correlated, yet there is no such correlation between $\partial h/\partial t$ and S_h , by showing that inertial waves interact with the buoyancy field in such a way as to induce a source S_h which adopts the same sign as the helicity in the local wave flux. Moreover, we have confirmed that, in simple model problems, the sign of h is simply determined by the direction of the wave flux. We conclude that the observed distributions of h and S_h in the numerical dynamos are consistent with the transport of helicity by waves.

The authors thank P.K. Yeung of Georgia Tech for sharing his DNS code and Uli Christensen and Johannes Wicht for many interesting discussion on core dynamics and for sharing their dynamo data set. The authors also thank the Leverhulme Trust for their generous support through the grant RPG-2015-195/RG77943.

References

- Bardsley O.P. & Davidson, P.A., 2016, Inertial-Alfven Waves as Columnar Helices in Planetary Cores. *J. Fluid Mech. (Rapids)*, **805** (online only).
- Bardsley O.P. & Davidson, P.A., 2017, The Dispersion of Magnetic-Coriolis Waves in Planetary Cores. *Geophys. J. Int.*, **210**(1), 18-26.
- Christensen, U. R., 2010, Dynamo scaling laws and application to the planets. *Space Sci. Rev.* **152**, 565-590.
- Christensen, U. R., 2011, Geodynamo models: Tools for understanding properties of Earth's magnetic field. *Phys. of Earth and Planetary Interiors*, **187**, 157-169.
- Christensen, U. R. & Wicht, J., 2007, Numerical dynamo simulations. In: *Treatise on Geophysics*, P. Olson Ed., Elsevier.

- Davidson, P. A., 2014, The dynamics and scaling laws of planetary dynamos driven by inertial waves, *Geophys. J Int.*, **198** (3), 1832-1847.
- Davidson, P. A. 2013, *Turbulence in rotating, stratified and electrically conducting fluids*. Cambridge University Press.
- Davidson, P. A. & Ranjan, A., 2015, Planetary Dynamos Driven by Helical Waves: Part 2, *Geophys. J Int.*, **202**, 1646-1662.
- Davidson, P.A., Staplehurst, P.J. & Dalziel, S.B., 2006, On the evolution of eddies in a rapidly rotating system. *J. Fluid Mech.*, **557**.
- Gilman, P. A., 1977. Nonlinear dynamics of Boussinesq convection in a deep rotating spherical shell. *Geophysical & Astrophysical Fluid Dynamics*, **8**(1), 93-135.
- Glatzmaier, G. A., & Olson, P., 1993. Highly supercritical thermal convection in a rotating spherical shell: centrifugal vs. radial gravity. *Geophysical & Astrophysical Fluid Dynamics*, **70**(1-4), 113-136.
- Greenspan, H. P., 1968, *The theory of rotating fluids*. Cambridge University Press.
- Hide, R., 1976, A note on helicity, *Geophys. Fluid Dyn.*, **7**, 157-61.
- Hide, R., Ibbetson, A. and Lighthill, M. J., 1968, On slow transverse flow past obstacles in a rapidly rotating fluid. *J. Fluid Mech.*, **32**, 251-272.
- Kageyama, A., Watanabe, K. & Sato, T., 1993. Simulation study of a magnetohydrodynamic dynamo: Convection in a rotating spherical shell. *Physics of Fluids B: Plasma Physics*, **5**(8), 2793-2805.
- Kitauchi, H., Araki, K. & Kida, S., 1997, Flow structure of thermal convection in a rotating spherical shell, *Nonlinearity*, **10**(4), 885
- Kono, M., Sakuraba, A. and Ishida, M., 2000. Dynamo simulation and palaeosecular variation models. *Phil. Trans. Royal Soc. London A*, **358**, pp.1123-1139.
- Loper, D.E., 2001. On the structure of a Taylor column driven by a buoyant parcel in an unbounded rotating fluid, *J. Fluid Mech.*, **427**, 131-165
- Moffatt, H. K. 1970, Dynamo action associated with random inertial waves in a rotating conducting fluid, *J. Fluid Mech.*, **44**(4).
- Moffatt, H. K. 1978, *Magnetic field generation in electrically conducting fluids*. Cambridge University Press.
- Olson, P., 1981. A simple physical model for the terrestrial dynamo, *J. Geophys. Res.*, **86**, 10875–10882.

- Olson P., Christensen, U. R. & Glatzmaier G. A., 1999, Numerical modelling of the geodynamo: mechanisms of field generation and equilibration. *J. Geophys. Res.*, **104** (B5), 10383.
- Ranjan A., 2017, Segregation of helicity in inertial wave packets. *Phys. Rev. Fluids*, **2**(3), 033801.
- Ranjan A. & Davidson P. A. 2014, Evolution of a turbulent cloud under rotation. *J. Fluid Mech.*, **756**, pp 488-509.
- Ranjan, A., Davidson, P. A., Christensen, U. R. & Wicht, J., 2018, Internally-driven inertial waves in geodynamo simulations. *Geophys. J. Int.*, **213**(2).
- Roberts, P. H. & King, E. M. 2013, On the genesis of the Earth's magnetism, *Rep. Prog. Phys.*, **76**(9).
- Sakuraba, A. & Roberts, P. H., 2009, Generation of a strong magnetic field using uniform heat flux at the surface of the core, *Nature Geoscience*, **2**, 802-805.
- Schaeffer, N., Jault, D., Nataf, H-C., & Fournier, A. 2017. Turbulent geodynamo simulations: a leap towards Earth's core. *Geophys. J. Int.* **211**, 1-29. doi: 10.1093/gji/ggx265
- Shimizu, H. & Loper, D.E., 2000. Small-scale helicity and α -effect in the Earth's core, *Phys. Earth planet. Inter.*, **121**, 139–155.
- Yadav, R. K., Gastine, T. & Christensen, U.R. 2013, Scaling laws in spherical shell dynamos with free-slip boundaries, *Icarus*, **225**, 184.
- Yeung, P. K. & Zhou, Y. 1998. Numerical study of rotating turbulence with external forcing, *Phys. Fluids*, **10**, 2895.